Journal of Intelligent Material Systems and Structures

Original article

Journal of Intelligent Material Systems and Structures
1–20

DOI: 10.1177/1045389X251374840
journals.sagepub.com/home/jim
Sage

Bias-flip synchronized switch damping technique for enhanced and adaptive vibration attenuation

Hao Tang[1] and Guobiao Hu[1]

Abstract

The synchronized switch damping (SSD) technique has garnered significant attention for its broadband efficacy and high performance. However, the low circuit quality of the SSD on inductor (SSDI) circuit and the instability issue associated with the SSD on voltage (SSDV) circuit limit their widespread applications. To address these issues, this study proposes an SSD on bias-flip (SSDBF) circuit. By incorporating a bias capacitor, the voltage inversion process is segmented into three phases through different LC loops, significantly enhancing the voltage inversion factor γ. Moreover, the bias voltage autonomously adjusts to the external excitation levels, eliminating the need for auxiliary monitoring and energy sources. A theoretical model and an equivalent circuit model (ECM) are developed to analyze the superiority of the SSDBF circuit across a wide frequency range. Both theoretical and simulation results demonstrate that the SSDBF circuit outperforms the traditional SSDI circuits, particularly in cases with low coupling coefficients and voltage inversion factors, while maintaining self-adaptivity across varying excitation conditions. Finally, experimental results validate the enhanced vibration attenuation and self-adaptivity of the SSDBF circuit, underscoring its great potential as a robust and efficient solution for advanced vibration control in various applications.

Keywords

synchronized switch damping, vibration control, bias-flip, electromechanical system

1. Introduction

Vibrations are commonly pervasive in mechanical structures and systems, which can lead to detrimental effects such as reduced fatigue life, decreased safety, and permanent damage (Lu et al., 2018; Shivashankar and Gopalakrishnan, 2020; Yan et al., 2022). To address this issue, researchers have proposed various vibration attenuation strategies, with the piezoelectric vibration control technology standing out as a widely favored solution due to its lightweight, simplicity, and compactness (Li et al., 2023; Sales et al., 2013). Specifically, piezoelectric vibration control strategies can be classified into two categories. The passive vibration control approach leverages the direct piezoelectric effect and converts vibrations into electricity, which is then dissipated through resistive or inductive circuits (Yamada et al., 2010). However, the passive technique suffers from the narrowband issue, and the resistive shunt has a relatively limited damping capability. Unlike the passive technique, active vibration control systems leverage the inverse piezoelectric effect and generally offer superior performance over a broadband frequency. However, active control systems are more complex in terms of implementation and energy-demanding, as the piezoelectric elements function as actuators to generate the control force needed to suppress vibrations (Aridogan and Basdogan, 2015; Gripp and Rade, 2018).

As a balanced alternative to the two aforementioned techniques, a semi-activate control strategy offers the advantages of simplicity and low cost while enhancing the overall damping effect. Still leveraging the direct piezoelectric effect, this approach is generally realized using synchronized switch damping (SSD) circuits in which synchronous instants are periodically triggered to enhance electrical damping (Qureshi et al., 2014). For example, the SSD on an inductor (SSDI) circuit

[1]Thrust of Internet of Things, The Hong Kong University of Science and Technology (Guangzhou), Guangzhou, Guangdong, China

Corresponding author:
Guobiao Hu, Internet of Things Thrust, The Hong Kong University of Science and Technology (Guangzhou), No.1 Duxue Road, Nansha District, Guangzhou, Guangdong 511453, China.
Email: guobiaohu@hkust-gz.edu.cn

(Richard et al., 1999, 2000) connects an inductor in parallel with the piezoelectric element, forming an LC oscillation at the displacement extrema. Through this mechanism, one can distort the voltage waveform and invert the polarity of the voltage across the piezoelectric element while also amplifying the voltage amplitude and creating a phase lag with the displacement. The amplified voltage and the associated phase lag cause the piezoelectric element to perform larger negative work on the system, thereby enhancing electrical damping and reducing the vibration amplitude. However, the SSDI circuit suffers from low circuit quality issues (Asanuma and Komatsuzaki, 2020; Zhang et al., 2019), resulting in a low voltage inversion factor and an unfavored slight voltage amplification as a significant portion of the energy is dissipated during the transfer process.

Studies have shown that external energy injection can enhance voltage inversion efficiency and electrical damping effect (Ji et al., 2016; Tang et al., 2025; Wu et al., 2019). The ideal scenario corresponds to an LC oscillation circuit loop with an infinitely large quality factor and 100% voltage inversion ratio. To this end, the SSD on voltage source (SSDV) circuit (Lefeuvre et al., 2006) was proposed, in which an external voltage source is incorporated into the LC oscillation loop to compensate for dissipated energy in the transfer process, thereby enhancing the electrical damping effect. However, a constantly supplied external voltage source may lead to overcompensation under low vibration conditions. As a result, the piezoelectric element may act as an actuator to excite the mechanical structure instead of suppressing it (Badel et al., 2006; Lallart et al., 2008). To address this issue, adaptive SSDV circuits were proposed (Ji et al., 2009a, 2009b; Wang et al., 2020) to accommodate varying vibration levels at different frequencies, thereby enhancing the vibration attenuation effect while preventing unexpected instability issues. Recently, Wu et al. (2022, 2024) proposed an SSD on energy injection (SSDEI) circuit, which achieved the voltage adjustment with a streamlined implementation utilizing a flyback topology (Wu et al., 2013). The injected energy into the system can be precisely controlled by presetting the synchronized switch period, thereby achieving an optimized voltage inversion ratio.

However, these approaches require additional monitoring and real-time algorithms to adjust the injected energy, which increases power consumption and adds complexity to the control system. More problematically, providing a stable and reliable energy source in practical applications is costly and technically challenging. To overcome these limitations, several multi-step strategies have been developed to increase the voltage inversion ratio in synchronized switching circuits without relying on external energy input. On this topic, the synchronized switch harvesting on capacitors (SSHC) circuit was proposed (Chen et al., 2017; Du and Seshia, 2017; Liu et al., 2020), in which energy transfer is achieved via charge neutralization using switched capacitors (SCs) instead of the LC oscillation with an inductor. The voltage inversion efficiency can be enhanced by incorporating multiple synchronized SCs, which allows more charge stored in C_p to be transferred into a series of capacitors, thereby re-charging C_p to a higher voltage level (Du et al., 2019). Due to the complexity of its operation and the need for precise time control, the SSHC technique is typically implemented on-chip. To ease timing constraints while achieving high voltage-flip efficiency, a multi-step bias-flip rectifier technique for piezoelectric energy harvesting was developed (Javvaji et al., 2019). Fabricated using a 130-nm CMOS process, the chip achieved a voltage-flip efficiency of 89.5% with only a 47 μH inductor used. These multi-step techniques are fundamentally based on the bias-flip mechanism, in which the bias capacitors serve as energy mediators, significantly enhancing operational efficiency without the need for external energy sources.

Building on the principles of multi-step and bias-flip, this work presents a novel SSD circuit on bias-flip (SSDBF) to enhance both vibration attenuation and system stability. In particular, a relatively large bias capacitor is incorporated into the LC oscillation loop as an internal energy reservoir, eliminating the need for an external energy source and simplifying the circuitry. Under a dedicated control strategy with four switches, the synchronous instant is divided into three stages, each corresponding to a distinct LC oscillation. In this process, the bias capacitor is charged in the first stage and discharged in the third, temporarily storing and returning the energy accumulated on the piezoelectric element. This mechanism leads to a stabilized bias voltage in the steady state. Notably, the SSDBF circuit exhibits self-adaptive capability (Liang et al., 2019; Zhao et al., 2021). When the vibration condition changes, a new charge-discharge equilibrium will be automatically established, as the energy accumulated in the bias capacitor is entirely sourced from the system's dynamics.

To demonstrate the enhanced performance of the proposed SSDBF circuit, a theoretical model is developed by extending the analysis of the traditional SSD circuits in both near- and off-resonant regions. Based on the theoretical model, the performance and superiority of the SSDBF are efficiently analyzed. The accuracy of the theoretical model is verified by an equivalent circuit model (ECM) established in the LTspice Software. The effectiveness of the SSDBF circuit in enhancing vibration attenuation and system stability is substantiated by the experimental results.

The rest of this article is organized as follows: In Section 2, the electromechanical model of a piezoelectric cantilever beam, the target structure for implementing vibration attenuation in this study, is presented, and

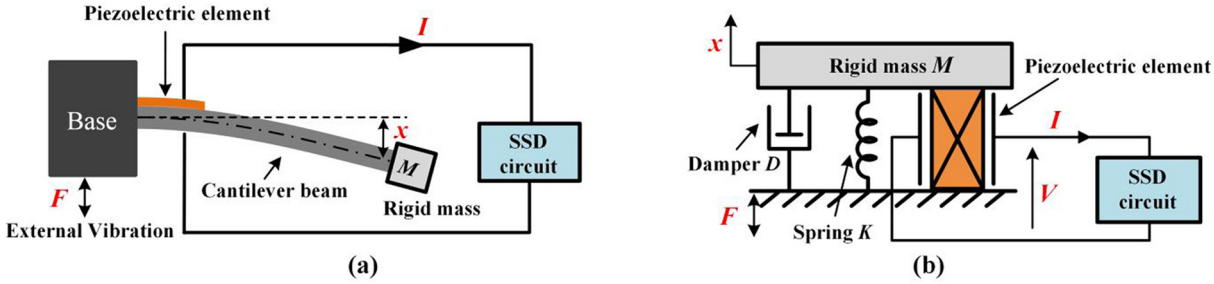

Figure 1. Schematic of electromechanical systems utilizing SSD circuits for vibration attenuation. (a) A piezoelectric cantilever beam; (b) An equivalent single-degree-of-freedom (SDOF) oscillator integrated with a piezoelectric element.

the working principles of the traditional SSDI and the proposed SSDBF circuits are explained and compared. In Section 3, an extended theoretical model for analyzing general SSD circuits is developed, and the effects of several system parameters on the vibration attenuation performance are studied. A comprehensive equivalent circuit model of the SSDBF circuit is established in Section 4 to verify the theoretical analysis and assess the performance improvement, followed by experimental validation presented in Section 5. Finally, Section 6 provides concluding remarks.

2. SSD techniques

This section introduces the traditional SSD technique and explains the working principle of the proposed SSDBF circuit. Beams are widely utilized in various engineering applications. In the low-frequency regime, a cantilever beam can often be represented using lumped parameters, typically modeled as a single-degree-of-freedom (SDOF) oscillator. For simplicity, in this study, a linear SDOF oscillator integrated with a piezoelectric element is adopted to characterize the electromechanical system targeted for vibration attenuation.

2.1. Electromechanical model

Figure 1(a) shows the schematic of the electromechanical system consisting of a piezoelectric beam and an SSD circuit. Figure 1(b) shows the corresponding equivalent SDOF model where M represents the equivalent mass, K is the spring stiffness, and D is the damping coefficient. The equivalent relationships between a piezoelectric cantilever beam and an SDOF oscillator integrated with a piezoelectric element have been extensively explored (Ji et al., 2018; Liang and Liao, 2012).

The structure is subjected to an external harmonic force F with an amplitude of F_M. x is the displacement of the oscillator. Then, the governing equation of the electromechanical model in the mechanical domain can be expressed as

$$M\ddot{x} + D\dot{x} + Kx + \alpha V = F \tag{1}$$

In the electrical domain, the piezoelectric element is modeled as a capacitive component with a capacitance of C_p. When subjected to varying stress, it generates a voltage V and outputs a current I. Then, the behavior of the piezoelectric element can be described as

$$I = \alpha\dot{x} - C_p\dot{V} \tag{2}$$

where α is the force-voltage factor of the piezoelectric element, which exerts a piezoelectric force on the oscillator to achieve the electromechanical coupling of the system. The coupling strength can be described by using the dimensionless coupling coefficient k^2, which is defined as the electrostatic energy divided by the total energy in the system when a quasi-static stress is applied on the piezoelectric beam (Badel and Lefeuvre, 2016). A modified coupling coefficient ${k_m}^2$, representing the ratio between the electrostatic and elastic energy, is also introduced to simplify the theoretical analysis (Lefeuvre et al., 2017). For weakly coupled electromechanical systems, the values of k^2 and ${k_m}^2$ are close to each other (Morel et al., 2018). It is worth noting that k^2 has a maximum value of 1, indicating that all the input mechanical energy is converted into electrostatic energy, while the value of ${k_m}^2$ is not constrained. The definitions of k^2, ${k_m}^2$, and their relationship are given as follows.

$$k^2 = \frac{\alpha^2}{\alpha^2 - KC_p}k_m^2 = \frac{\alpha^2}{KC_p} = \frac{k^2}{1-k^2} \tag{3}$$

The natural angular frequency ω_0 of the electromechanical oscillator under the short-circuit condition is given as

$$\omega_0 = \sqrt{\frac{K}{M}} \tag{4}$$

Furthermore, the mechanical quality factor Q_m and the normalized frequency Ω of the electromechanical system are defined as

$$Q_m = \frac{\sqrt{MK}}{D}\Omega = \frac{\omega}{\omega_0} \tag{5}$$

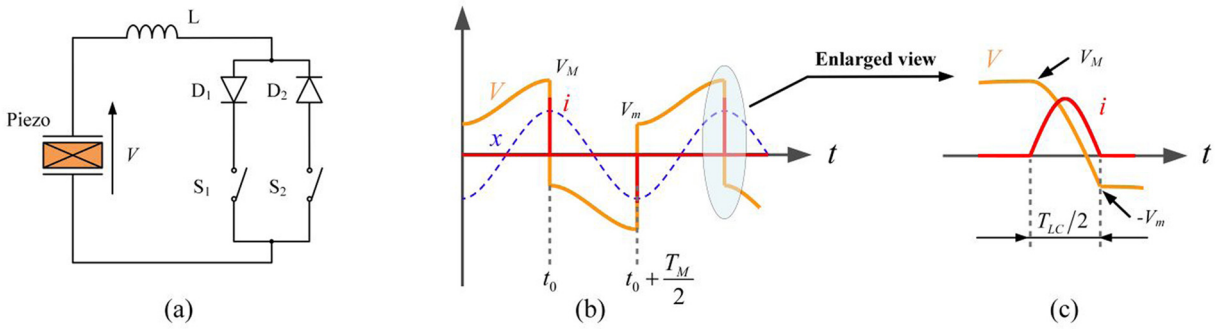

Figure 2. (a) Topology of the SSDI circuit, (b) working waveforms of the SSDI circuit, and (c) enlarged view of the synchronous instants of the SSDI circuit.

When the system is in open-circuit, the current I in equation (2) is zero. The piezoelectric voltage V is in phase with the displacement x, leading to:

$$\alpha\dot{x} = C_p\dot{V} \tag{6}$$

Substituting equation (6) into equation (1) yields

$$M\ddot{x} + D\dot{x} + (K + \frac{\alpha}{C_p})x = F \tag{7}$$

Hence, the open-circuit stiffness of the electromechanical oscillator is obtained by

$$K_{oc} = K + \frac{\alpha}{C_p} \tag{8}$$

Substituting equation (8) back into equation (4), and combining with equation (5) and equation (3), the open-circuit normalized resonant frequency can be derived as

$$\Omega_{oc} = \sqrt{1 + k_m^2} \tag{9}$$

The displacement amplitude of the electromechanical oscillator under open-circuit conditions can then be easily calculated by applying the Fourier transform to equation (7), resulting in

$$x_{M\_OC} = \frac{F_M}{\sqrt{(K - M\omega^2 + \frac{\alpha^2}{C_p})^2 + (D\omega)^2}} \tag{10}$$

2.2. SSD technique

Figure 2(a) demonstrates the traditional SSDI circuit, which consists of an inductor L, two switches, and two diodes. The two switches typically remain open and only close when the displacement x reaches its positive or negative extremum. At these instants, an LC oscillation loop is formed with an LC period of $T_{LC} = 2\pi\sqrt{LC_{\text{eq}}}$, allowing rapid energy exchange between the piezoelectric capacitor and the inductor. After a half period of the LC oscillation, the polarity of the voltage across the piezoelectric element is completely inversed. Defining the voltages across the piezoelectric element before and after the synchronous instants are V_M and $-V_m$ related as follows.

$$V_m = \gamma V_M \tag{11}$$

where γ is the voltage inversion factor, of which the value ranges between 0 and 1 due to unavoidable electrical dissipation during the LC oscillation. As each switching-on duration is half of an LC cycle, that is, $T_{on} = T_{LC}/2 = \pi\sqrt{LC_{\text{eq}}}$, the voltage inversion factor can be related to the circuit quality factor Q_I (Liang and Chung, 2013) as

$$\gamma = e^{-\pi/(2Q_I)} \tag{12}$$

The circuit quality factor Q_I characterizes the energy dissipation during the LRC half-cycle associated with each synchronized switching loop. It is defined as the ratio of the energy stored to the energy dissipated in a single LRC oscillation cycle. Specifically, it can be expressed as:

$$Q = \frac{1}{\mathrm{r}}\sqrt{\frac{L}{C_{eq}}} \tag{13}$$

where r, L, and C_{eq} are the parasitic resistance, inductance, and equivalent capacitance involved in each LC oscillation loop, respectively. A higher value of γ or Q_I indicates a more efficient synchronized switching circuit, as less energy is dissipated due to parasitic effects (Morel et al., 2022b; Tian et al., 2021; Wu et al., 2022).

In the open-circuit condition, the piezoelectric voltage varies proportionally with the displacement, establishing an additional relationship between the two voltages as

$$V_M = V_m + \frac{2\alpha}{C_p}x_M \tag{14}$$

where, x_M denotes the displacement amplitude of the oscillator when the SSD circuits shunts to the piezoelectric element. Solving equation (11) and equation (14)

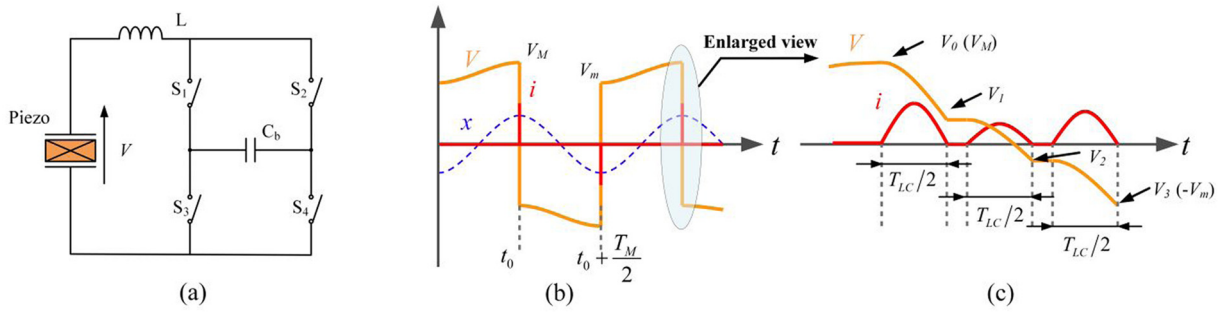

Figure 3. (a) Topology of the SSDBF circuit, (b) working waveforms of the SSDBF circuit, and (c) Enlarged view of the synchronous instant of the SSDBF circuit.

simultaneously yields the solutions for V_M and V_m as follows

$$\begin{cases} V_M = \frac{1}{1-\gamma}\frac{2\alpha}{C_p}x_M \\ V_m = \frac{\gamma}{1-\gamma}\frac{2\alpha}{C_p}x_M \end{cases} \tag{15}$$

It can be found in equations (11) and (15) that the electrical efficiency of the SSDI circuit is limited by the voltage inversion factor γ. A smaller γ indicates that a larger proportion of the electrostatic energy is converted into electrical dissipation, resulting in a reduced voltage inversion ratio and a decrease in the magnified voltage amplitude, thereby weakening the electrical damping effect. From the above analysis, it is evident that increasing the voltage inversion factor γ can improve the vibration attenuation performance of the SSD technique (Qureshi et al., 2015).

2.3. SSDBF circuit

For the aforementioned reasons, an SSD on bias-flip (SSDBF) circuit is proposed for enhanced vibration attenuation while maintaining adaptability to varying vibration conditions. Figure 3(a) shows the schematic of the SSDBF circuit, which consists of an inductor, a bias capacitor, and four switches. Since the LC oscillation period T_{LC} is much smaller than the mechanical oscillation period T_M, the working waveforms of the SSDBF circuit shown in Figure 3(b) closely resemble those of the traditional SSDI circuit, except for a larger voltage ratio between V_m and V_M. Figure 3(c) displays the enlarged view of the synchronous instant, highlighting three LC oscillations, each with a time period of $T_{LC}/2$. Note that the voltage depicted in Figure 3 represents the voltage across the piezoelectric element.

Figure 4 shows the working phases of the SSDBF circuit at the synchronous instants, which are accomplished by conducting bias-flip actions through three different LC oscillation loops within a cycle of T_M. The first (a–c) and second (d–f) rows, respectively, depict the three bias-flip actions executed at the positive and negative displacement maxima. Figure 4(a) shows the first LC oscillation loop formed by C_p-L-S_1-C_b-S_4 when the displacement reaches its positive maxima. After half of the LC oscillation period T_{LC}, the voltage on C_p flips from V_0 to V_1. The bias capacitor C_b is charged in this process. Then, the second LC oscillation loop is immediately formed by C_p-L-S_2-S_4, as shown in Figure 4(b), and the first LC oscillation loop is disconnected. Note that the connection and disconnection of the LC oscillation loops are realized by controlling the four switches. After undergoing a second-phase LC oscillation for another $T_{LC}/2$, the piezoelectric voltage flips to a negative value of V_2. During this process, C_b is not engaged in the second LC oscillation loop and retains its voltage V_b. The third LC oscillation loop is formed by C_p-L-S_2-C_b-S_3, as shown in Figure 4(c). During this process, the current flows out from C_b, inversely charging C_p and leading to a more negative voltage V_3. Following a similar operating pattern, the synchronous instant during the negative half cycle is achieved by three other different loops, as depicted in Figure 4(d) to (f). The bias capacitor C_b is also charged in the first phase and discharged in the third phase. It is worth mentioning that, theoretically, there is no requirement for setting a time interval between each LC oscillation, as they are conducted in separate switching loops. However, in practical implementation, an interval on the order of tens of microseconds is recommended to ensure the independence of each LC oscillation.

The value of C_b should be selected to be significantly larger than that of C_p. As a result, during the LC oscillations, the bias capacitor C_b behaves as a quasi-DC voltage source and stabilizes at a bias voltage V_b in the steady state. The amount of energy transferred through C_b during the first and third bias-flips is nearly identical, which can be estimated by the product of the change in piezoelectric charge and V_b (Zhao et al., 2021), as described by equation (16).

$$C_p(V_0 - V_1)V_b = C_p(V_2 - V_3)V_b \tag{16}$$

In the first and third LC oscillations, C_b is connected in series with C_p, resulting in an equivalent capacitance $C_{eq} = ({C_p}^{-1} + {C_b}^{-1})^{-1}$. Given that $C_b >> C_p$, one

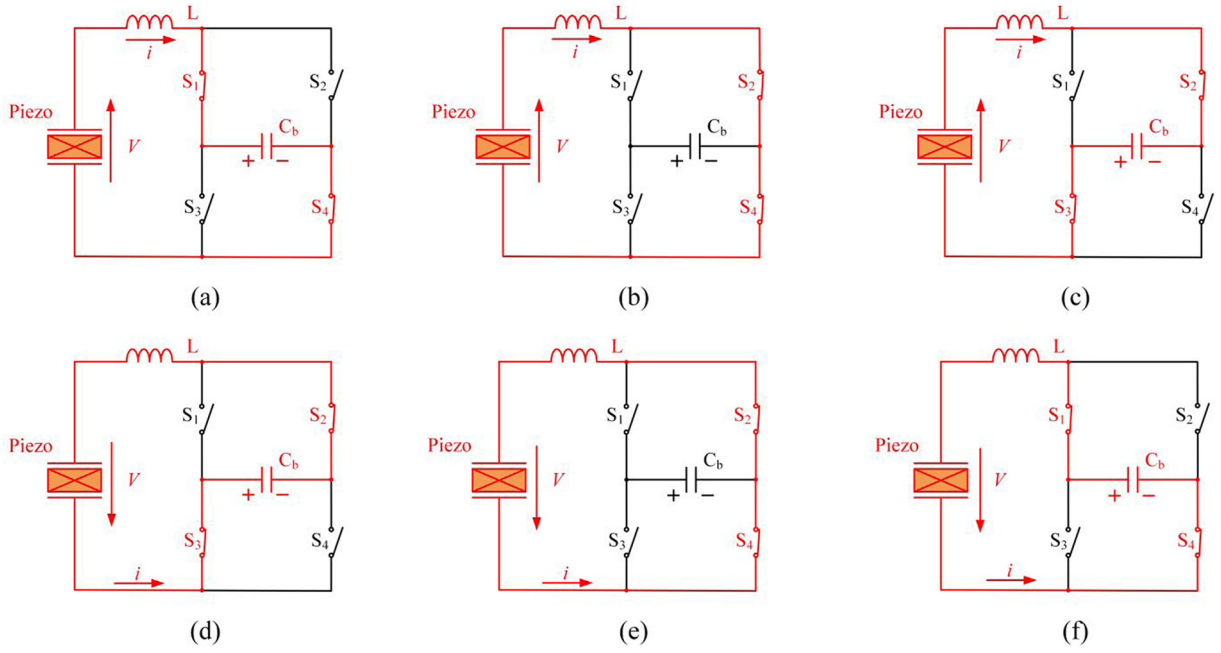

Figure 4. Working phases of the SSDBF circuit at synchronous instants. (a–c) LC oscillation loops for the positive vibration cycle; (d–f) LC oscillation loops for the negative vibration cycle.

easily derives $C_{eq} \approx C_p$. Therefore, it is reasonable to adopt a uniform voltage inversion factor γ for all three bias-flips for simplicity. Based on this assumption, the voltage relationships among V_0, V_1, V_2, and V_3 during the three bias-flips in the SSDBF circuit are described as

$$\begin{cases} \gamma(V_0 - V_b) = -(V_1 - V_b) \\ \gamma V_1 = -V_2 \\ \gamma(V_2 + V_b) = -(V_3 + V_b) \end{cases} \tag{17}$$

By combining equations (11) and (17), an equivalent inversion factor γ_{eq} for the SSDBF circuit can be defined as

$$\gamma_{eq} = \frac{V_m}{V_M} = -\frac{V_3}{V_0} = \frac{2\gamma + 1}{\gamma + 2} \tag{18}$$

Equation (18) shows that the SSDBF circuit can achieve a larger equivalent inversion factor γ_{eq} compared with the SSDI circuit, which indicates reduced electrical dissipation during the LC oscillations. This results in a more significantly magnified voltage amplitude, together with the phase lag effect, thereby producing more negative work and a stronger electrical damping effect.

3. Theoretical analysis

The SSD circuit analyses are typically conducted using the in-phase model for simplicity, but the accuracy is limited to frequencies near resonance (Badel et al., 2006; Wu et al., 2022). This section first introduces a universally accurate model for the SSD circuits applicable over a wide frequency range. Then, based on the model, it examines the effects of several dimensionless parameters on the vibration attenuation performance of the SSD circuits.

3.1. Universal model for SSD circuits

Assuming that the base is excited by a harmonic force with a magnitude of F_M, there will be a phase angle φ between the applied force and displacement (Tang and Yang, 2011), that is

$$\begin{cases} F = -F_M \cos(\omega t + \varphi) \\ x = -x_M \cos(\omega t) \end{cases} \tag{19}$$

Multiplying both sides of equation (1) and equation (2) by the velocity, and integrating them with respect to the time variable, two energy balance equations can then be obtained.

$$\int F\dot{x}dt = \frac{1}{2}M\dot{x}^2 + \frac{1}{2}Kx^2 + \int D\dot{x}^2 dt + \int \alpha V\dot{x}dt \tag{20}$$

$$\int \alpha V\dot{x}dt = \frac{1}{2}C_p V^2 + \int VIdt \tag{21}$$

The left-hand side (LHS) of equation (20) represents the input energy generated by the work done by the force F. The terms on the right-hand side (RHS) denote the potential energy, kinetic energy, mechanical loss due to the damping effect, and the energy converted

into electrical form by the piezoelectric element, respectively. Specifically, the last term can be further decomposed into two components, as given in equation (21). The two components on the RHS of equation (21) represent the electrostatic energy stored in the piezoelectric element and the energy dissipated by the SSD circuits.

The integrals in equations (20) and (21) are evaluated over half of a vibration period, that is, from t_0 to $t_0 + T_M/2$, in Figures 2(b) and 3(b). At the beginning and end of this half period, the displacement of this electromechanical oscillator reaches the maxima, which indicates that the kinetic energy is zero and the potential energy is maximum. Therefore, it is easily understood that the input energy over this half period only flows into the mechanical loss and the converted energy. For the SSDI circuit, the converted energy can be expressed as

$$E = \frac{1}{2}C_p(V_M^2 - V_m^2) = \frac{1+\gamma}{1-\gamma}\frac{2\alpha^2}{C_p}x_M^2 \tag{22}$$

Based on the above analysis and by combining equation (22) and equation (20), we obtain

$$\int F\dot{x}dt = \int D\dot{x}^2dt + \frac{1+\gamma}{1-\gamma}\frac{2\alpha^2}{C_p}x_M^2 \tag{23}$$

Substituting equation (22) into equation (23) and integrating over $[t_0, t_0 + T_M/2]$ gives

$$F_M \sin(\varphi) = D\omega x_M + \frac{1+\gamma}{1-\gamma}\frac{4\alpha^2}{C_p}x_M \tag{24}$$

The second relationship between F_M and φ is found by differentiating equation (1) with respect to time t as described by equation (25).

$$M\frac{d}{dt}\ddot{x} + D\frac{d}{dt}\dot{x} + K\frac{d}{dt}x + \alpha\dot{V} = \frac{d}{dt}F \tag{25}$$

Since the system remains in the open-circuit condition during the period from t_0 to $t_0 + T_M/2$, the current I in equation (2) is thus zero. Substituting equation (2) into equation (25), we have

$$M\frac{d}{dt}\ddot{x} + D\frac{d}{dt}\dot{x} + \left(K + \frac{\alpha^2}{C_p}\right)\frac{d}{dt}x = \frac{d}{dt}F \tag{26}$$

Integrating equation (26) over $[t_0, t_0 + T_M/2]$ yields

$$F_M \cos(\varphi) = \left(K - M\omega^2 + \frac{\alpha^2}{C_p}\right)x_M \tag{27}$$

Finally, the displacement amplitude of the electromechanical oscillator connected to the SSDI circuit can be calculated by summing the squares of equations (24) and (27). Following a bit of more mathematical processing, one obtains

$$x_{M\_SSDI} = \frac{F_M}{\sqrt{\left(K - M\omega^2 + \frac{\alpha^2}{C_p}\right)^2 + \left(D\omega + \frac{1+\gamma}{1-\gamma}\frac{4}{\pi}\frac{\alpha^2}{C_p}\right)^2}} \tag{28}$$

To fairly compare the vibration attenuation performance of different SSD circuits, we define a normalized displacement amplitude x_{norm}, which is the ratio of the displacement amplitude for the case using an SSD circuit to that of the open-circuit case. Dividing equation (28) by equation (10) gives the expression of x_{norm} for the SSDI circuit.

$$x_{norm\_SSDI} = \frac{\sqrt{\left(1 - \Omega^2 + k_m^2\right)^2 + \left(\frac{\Omega}{Q_m}\right)^2}}{\sqrt{\left(1 - \Omega^2 + k_m^2\right)^2 + \left(\frac{\Omega}{Q_m} + \frac{1+\gamma}{1-\gamma}\frac{4}{\pi}k_m^2\right)^2}} \tag{29}$$

The normalized displacement amplitude for the case using an SSDBF circuit can be determined by substituting equation (18) into equation (29).

$$x_{norm\_SSDBF} = \frac{\sqrt{\left(1 - \Omega^2 + k_m^2\right)^2 + \left(\frac{\Omega}{Q_m}\right)^2}}{\sqrt{\left(1 - \Omega^2 + k_m^2\right)^2 + \left(\frac{\Omega}{Q_m} + \frac{1+\gamma}{1-\gamma}\frac{12}{\pi}k_m^2\right)^2}} \tag{30}$$

Moreover, the parameter Δx_{norm} is defined in equation (31) to evaluate the enhanced vibration attenuation performance of the SSDBF circuit compared to the SSDI circuit by referencing the displacement amplitude under the open-circuit condition. The absolute difference directly reflects the reduction in the normalized displacement amplitude x_{norm} and avoids potential misleading interpretation caused by ratio-based comparisons, especially in the off-resonance region where the baseline displacement under the open-circuit condition is very small.

$$\triangle x_{norm} = x_{norm\_SSDI} - x_{norm\_SSDBF} \tag{31}$$

3.2. Influences of dimensionless parameters

By using the dimensionless parameters defined in equations (3) and (5), that is, quality factor Q_m and electromechanical coupling coefficient ${k_m}^2$, one can transform the original equations governed by parameters, such as the mass M, stiffness K, and damping coefficient D, into a dimensionless form governed by parameters of ${k_m}^2$, Q_m, and γ. In fact, the solutions presented in equations (29) and (30) are already in the dimensionless form. On the one hand, the expressions are significantly simplified, making them easier to interpret and solve. On the other hand, this ensures that the results are universally applicable across systems of different scales.

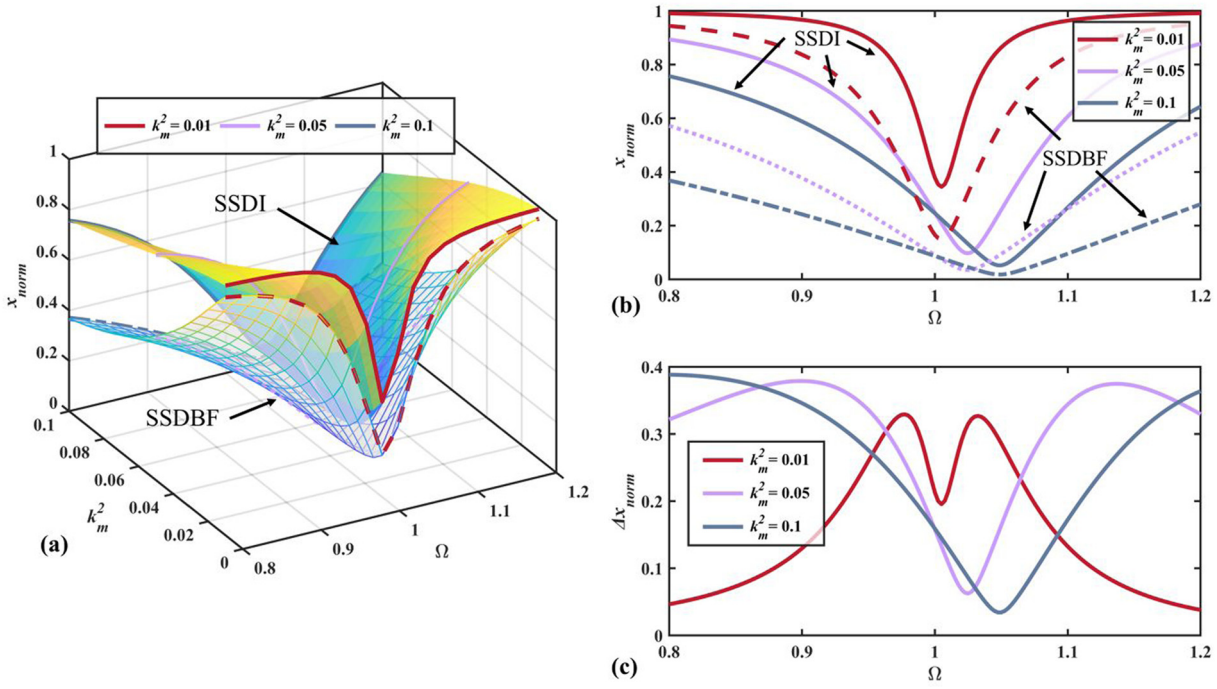

Figure 5. Given γ = 0.5 and Q_m = 50: (a) normalized displacement magnitude x_{norm} versus normalized frequency Ω and coupling coefficient factor k_m^2, (b) normalized displacement magnitude versus normalized frequency for the SSDI and SSDBF circuits in the weak, medium, and strong coupling conditions, and (c) Δx_{norm} versus normalized frequency in the weak, medium and strong coupling conditions.

3.2.1. Electromechanical coupling coefficient k_m^2. k_m^2 is a parameter that characterizes the coupling strength and energy conversion capability of the electromechanical system. A larger k_m^2 indicates a stronger electromechanical coupling, allowing a greater proportion of the input energy to be converted into electrostatic energy. Moreover, k_m^2 also indicates the maximum electrical damping of the electromechanical system because the SSD circuits can regulate the voltage to conduct negative work, thereby producing an electrical damping effect (Tian et al., 2021).

Figure 5(a) plots the normalized displacement amplitude x_{norm} versus the normalized frequency Ω and the coupling coefficient k_m^2, when using the SSDI and SSDBF circuits for vibration attenuation. The voltage inversion factor γ and the mechanical quality factor Q_m are set to 0.5 and 50, respectively. Notably, x_{norm} is smaller when using the SSDBF circuit compared to the SSDI circuit across the whole range of Ω and k_m^2, indicating that the SSDBF circuit can better attenuate vibration. In addition, for the SSDBF circuit, x_{norm} decreases significantly with the increase of k_m^2, whereas for the SSDI circuit, it exhibits a relatively smaller variation.

To more clearly illustrate the vibration attenuation effect, Figure 5(b) and (c) present x_{norm} and Δx_{norm} when employing the SSDI and SSDBF circuits at three different k_m^2, respectively, representing the weak (k_m^2 = 0.01), medium (k_m^2 = 0.05), and strong (k_m^2 = 0.1) coupling conditions. The minimum x_{norm} is achieved at the open-circuit resonant frequency (Ω_{oc}) in Figure 5(b), which indicates that SSD circuits perform most effectively near resonance. Besides, they can help decrease x_{norm} across a broad frequency range in strongly coupled systems because more converted electrostatic energy can enhance the electrical damping effect. Moreover, as shown in Figure 5(c), in the near-resonance region, the weakly coupled system (k_m^2 = 0.01) exhibits two peaks of Δx_{norm}, occurring at two different frequencies symmetrically positioned around Ω_{oc}, and Δx_{norm} is relatively small in the off-resonance region, indicating that the enhancement brought by the SSDBF circuit is pretty limited. In contrast, for moderately and strongly coupled systems, Δx_{norm} reaches its minimum at Ω_{oc} (slightly above Ω = 1), indicating less enhancement brought by the SSDBF circuit, whereas more significant improvements are observed in the off-resonance region.

3.2.2. Mechanical quality factor Q_m. The mechanical quality factor Q_m is a parameter that characterizes the intrinsic damping behavior of the electromechanical system. A lower Q_m indicates higher mechanical damping D and greater mechanical loss, resulting in

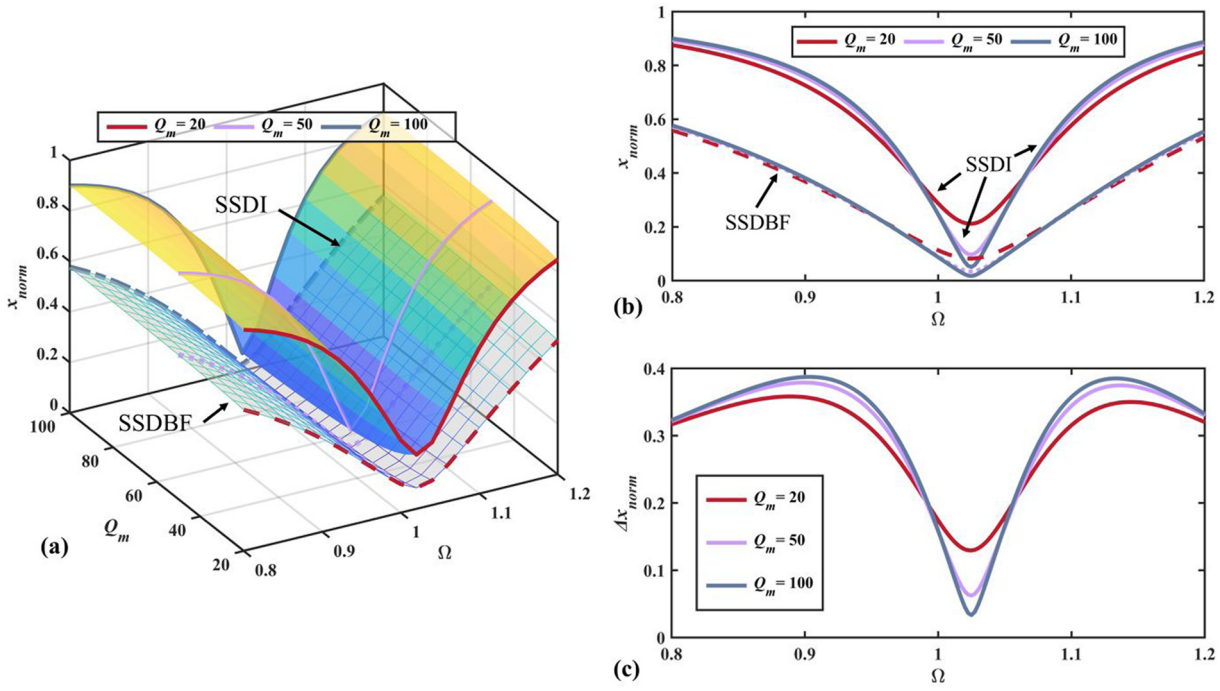

Figure 6. Given $\gamma = 0.5$ and $k_m^2 = 0.05$: (a) normalized displacement magnitude x_{norm} versus normalized frequency Ω and mechanical quality factor Q_m, (b) Normalized displacement magnitude versus normalized frequency for the SSDI and SSDBF circuits under $Q_m = 20$, $Q_m = 50$, and $Q_m = 100$, and (c) Δx_{norm} versus normalized frequency under $Q_m = 20$, $Q_m = 50$, and $Q_m = 100$.

decreased displacement amplitude. Previous studies (Brenes et al., 2020; Morel et al., 2022a) have shown that when employing synchronous switching circuits for energy harvesting, achieving maximum harvested power requires the electrical damping to match the mechanical damping. Therefore, researchers have explored electrical-based tunable piezoelectric vibration energy harvesting techniques to achieve damping matching. The results suggest that the amount of harvested energy is intricately influenced by the interplay between electrical and mechanical damping (Morel et al., 2022a). However, since the primary objective of this study is vibration attenuation, the SSD circuits are expected to generate the maximum electrical damping to enhance the vibration attenuation effect.

Figure 6(a) compares the normalized displacement magnitude x_{norm} versus the normalized frequency Ω and the mechanical quality factor Q_m when utilizing the SSDI and SSDBF circuits. The voltage inversion factor γ and the coupling coefficient k_m^2 are set to 0.5 and 0.05 (medium coupling strength), respectively. Similar to the observation in Figure 5(a), x_{norm} is consistently lower when using the SSDBF circuit than the SSDI circuit. However, unlike k_m^2, increasing Q_m does not significantly influence x_{norm} for the SSDI and SSDBF circuits. This phenomenon suggests that the electrical damping produced by the two SSD circuits significantly surpasses the intrinsic mechanical damping of the moderately coupled system with $k_m^2 = 0.05$.

Figure 6(b) provides a clear view of x_{norm} when employing the SSDI and SSDBF circuits for systems with high ($Q_m = 100$), medium ($Q_m = 50$), and low ($Q_m = 20$) mechanical quality factors. For both SSDI and SSDBF circuits, varying Q_m has little influence on x_{norm} in the off-resonance region. However, when using the SSDI circuit, x_{norm} decreases in the near-resonance region for the system with a large Q_m, while x_{norm} for the SSDBF circuit is still insensitive to Q_m. Moreover, as revealed in Figure 6(c), the improvement of the SSDBF circuit, represented by Δx_{norm}, is not significantly affected by Q_m, except in the region near Ω_{oc}, where a smaller Q_m results in a more remarkable enhancement of the SSDBF circuit compared to the SSDI circuit.

3.2.3. Voltage inversion factor γ. The inversion factor γ is an essential metric for evaluating the electrical efficiency of the synchronous switching circuit. During the inversion process, a portion of energy is dissipated due to the parasitic resistance, which reduces the voltage amplitude and, consequently, weakens the electrical damping effect. The circuit quality factor Q_I, defined in equation (11), also provides a measure of the electrical

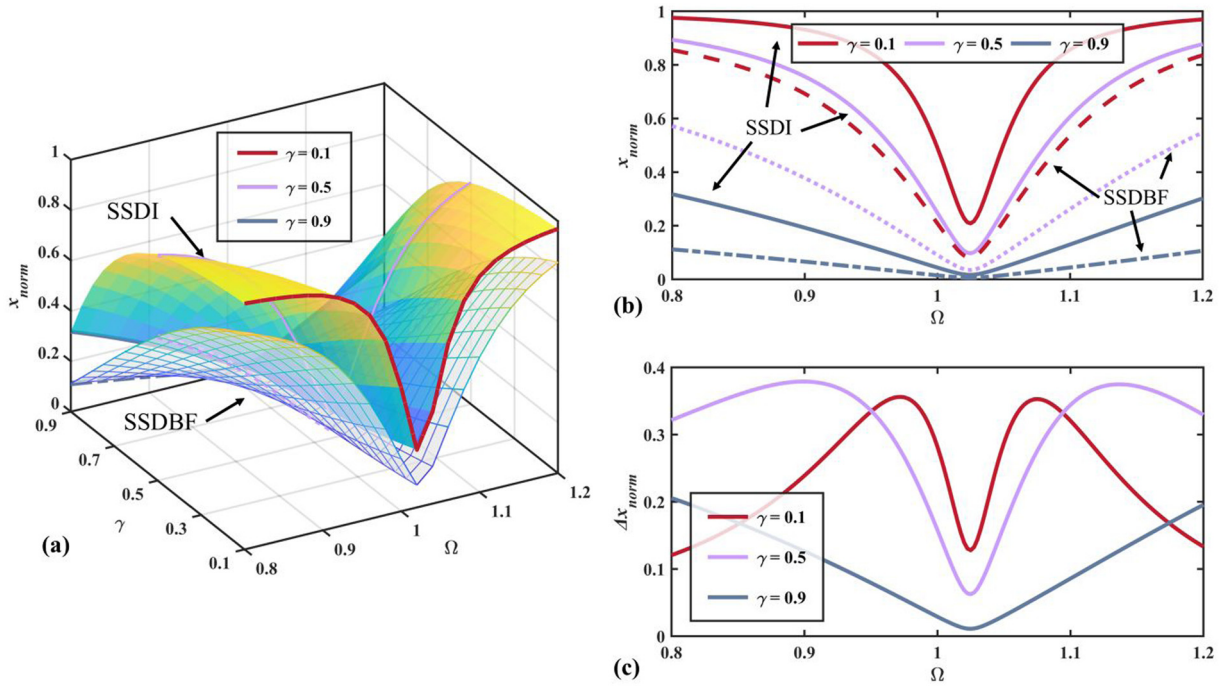

Figure 7. Given $k_m^2 = 0.05$ and $Q_m = 50$: (a) normalized displacement magnitude x_{norm} versus normalized frequency Ω and voltage inversion factor γ, (b) normalized displacement magnitude versus normalized frequency for the SSDI and SSDBF circuits under $\gamma = 0.1$, $\gamma = 0.2$, and $\gamma = 0.9$, and (c) Δx_{norm} versus normalized frequency under $\gamma = 0.1$, $\gamma = 0.2$, and $\gamma = 0.9$.

efficiency, with its relationship to the inversion factor γ described in the same equation.

Figure 7(a) presents the normalized displacement magnitude x_{norm} versus the normalized frequency Ω and the voltage inversion factor γ for the SSDI and SSDBF circuits. The coupling coefficient k_m^2 and the mechanical quality factor Q_m are set to 0.05 (medium coupling strength) and 50, respectively. One can note in the figure that x_{norm} for both SSDI and SSDBF circuits gradually decreases as γ increases. This is because less electrical energy is dissipated during the voltage inversion process. As a result, a larger portion of electrostatic energy is utilized by the SSD circuits to produce a stronger electrical damping effect.

Figure 7(b) shows x_{norm} for the SSDI and SSDBF circuits across three different γ values, and Figure 7(c) depicts the corresponding Δx_{norm} for the SSDBF circuit. It is noteworthy that compared to the SSDI circuit, the enhancement provided by the SSDBF circuit, as reflected by Δx_{norm}, is more pronounced in the off-resonance region for $\gamma = 0.5$ and $\gamma = 0.9$ cases, with Δx_{norm} decreases in the near-resonance region. For a smaller $\gamma = 0.1$, Δx_{norm} displays two peaks, with a valley observed at Ω_{oc} point. Apart from these two peaks, Δx_{norm} decreases in the off-resonant region, indicating reduced enhancement.

From a holistic perspective, the inversion factor γ and the coupling coefficient k_m^2 have similar influences on the performance of the SSDI and SSDBF circuits. Specifically, both SSDI and SSDBF circuits achieve greater vibration attenuation effects with higher values of γ or k_m^2 as the voltage amplitude is further amplified and more electrostatic energy is utilized to produce a stronger electrical damping effect. However, the improvement provided by the SSDBF circuit in the near-resonance region is less significant. On the other hand, smaller γ or k_m^2 contributes to more remarkable improvements of the SSDBF circuit than the SSDI circuit, especially in the near-resonant region. In contrast, Q_m has little influence on the performance of the SSD circuits, as the electrical damping dominates and typically exceeds the mechanical damping effect.

4. Simulation verification

To evaluate and verify the performance of the SSDBF circuit, a simulation model is built in LTspice™ using an ECM representation (Hu et al., 2022; Wang et al., 2025). The SSDBF circuit is directly implemented with ideal switches provided in the software to eliminate unexpected energy losses. The parameters of the simulation model are listed in Table 1.

4.1. Model establishment

The damper (D), mass (M), and spring (K)in the mechanical domain are analogous to the resistor (R), inductor (L), and capacitor (C)in the electrical domain,

Table 1. Parameters of the simulated electromechanical oscillator.

Variable	Value	Variable	Value
M	9.32g	α	5.56e-4 N/V
D	0.01148 N.s/m	L	470 μH
K	358.82 N/m	r	50 Ω
C_p	43.3 nF	C_b	10 μF

respectively. Similarly, the velocity and displacement correspond to the current and charge, respectively. A force excitation is equivalent to a voltage source. Moreover, the electromechanical coupling of the piezoelectric element is simulated by using arbitrary behavioral voltage and current sources, with the control functions defined according to the terms αV and $\alpha\dot{x}$ in equations (1) and (2).

The SSDBF circuit is directly implemented in the circuit simulation software. The control strategy of the SSDBF circuit is realized by four ideal switches with the corresponding control signals shown in Figure 8(c). The resistor R_1 with a value of r is introduced to account for the electrical dissipation in the LC oscillation. It plays a crucial role in determining the inversion factor (γ) of the LC oscillation circuit. Moreover, Figure 8(b) shows an ideal peak detection circuit (Shareef et al., 2019) that can change the level of detection voltage V_{dect} at the displacement extrema. Then, the corresponding rising and falling edges will trigger the switch control signal to initiate the bias flips processes. Unlike the SSDBF circuit, the SSDI circuit topology is much simpler. It can be built by using two ideal switches without the need for a bias capacitor.

4.2. Results and discussion

Figure 9 presents the simulated steady-state voltage waveforms of the SSDI and SSDBF circuits at the open-circuit resonant frequency Ω_{oc} and under an acceleration of 0.5g. By analyzing V_M and V_m in Figure 9(b) and (d), followed by post-processing, the voltage inversion factors of the SSDI and SSDBF circuits are calculated to be 0.448 and 0.781, respectively. the bias voltage stabilizes at $V_b = 29.98$ V, which play a crucial role in improving the inversion factor. The higher inversion factor implies that the mechanical produces a smaller displacement amplitude, as the voltage difference in open-circuit is proportional to x_M, according to equation (14). Moreover, reduced current peaks are observed in the SSDBF circuit, decreasing from 0.546 to 0.198 mA. The decrease in current peaks reduces electrical dissipation in LC oscillations, resulting in

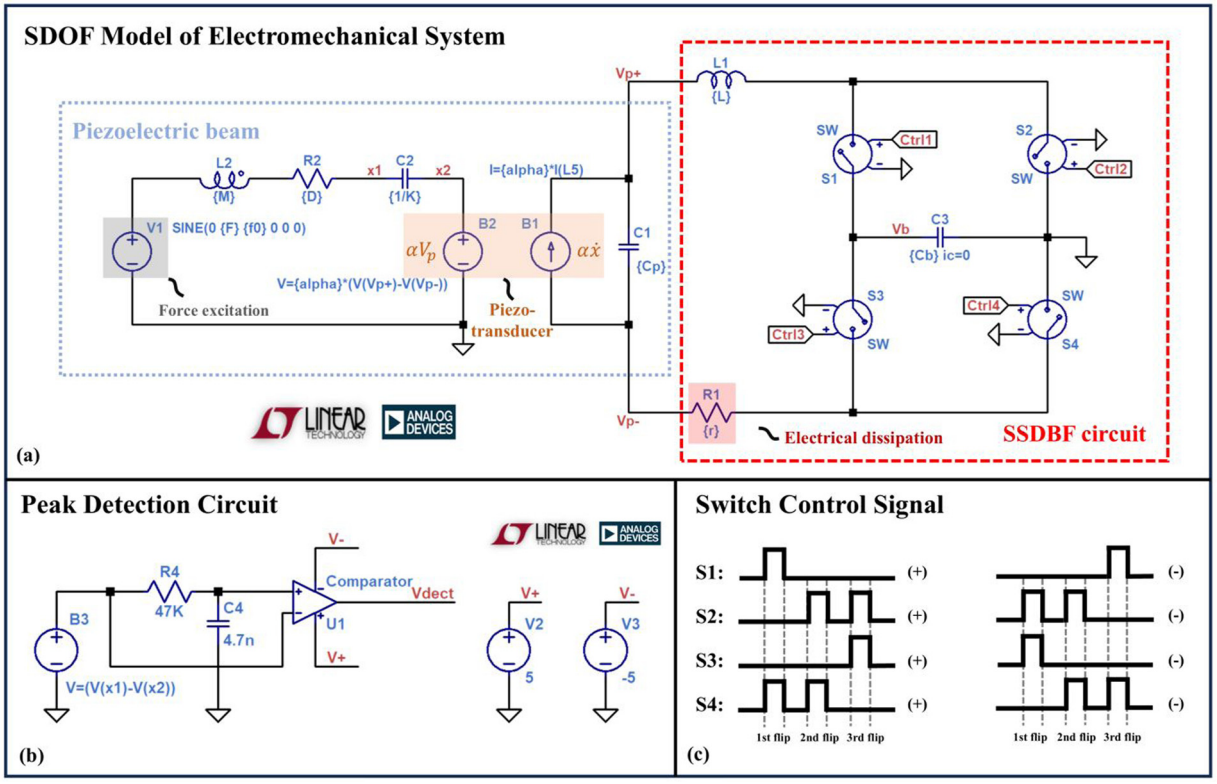

Figure 8. (a) The schematic of the electromechanical system connected to the proposed SSDBF circuit in LTspice™ Software, (b) peak detection circuit, and (c) switch control signals.

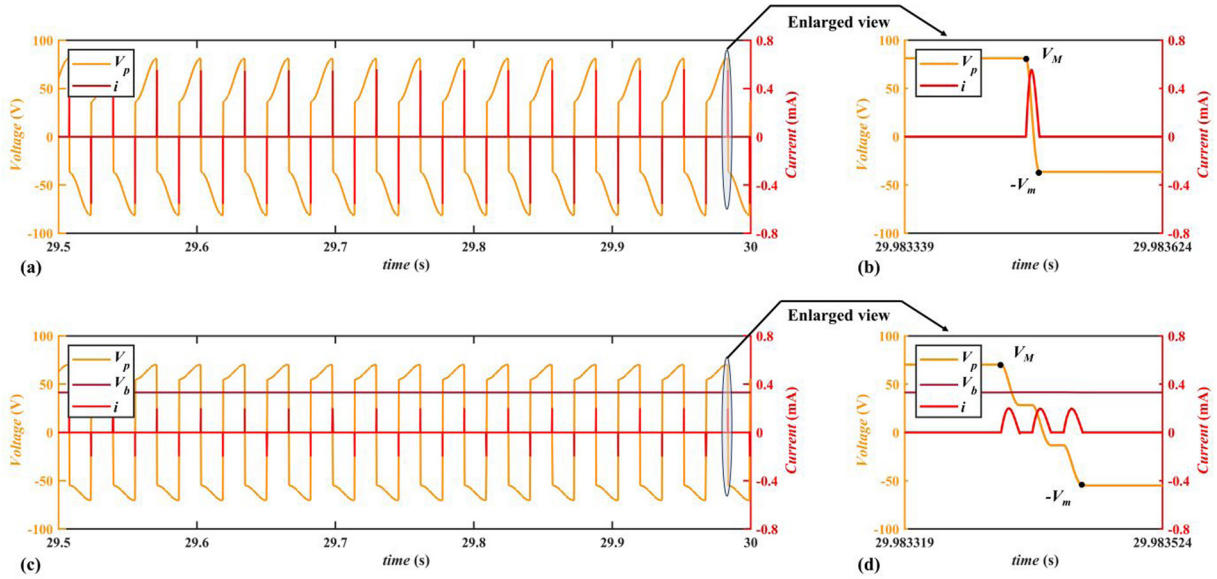

Figure 9. The simulated working waveforms of the SSDI and SSDBF circuits. (a and b) Voltage and current waveforms of the SSDI circuit; (c and d) Voltage and current waveforms of the SSDBF circuit.

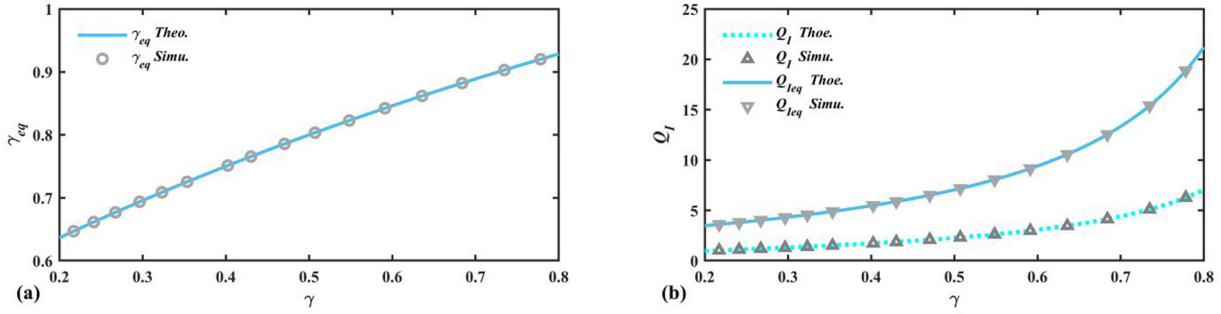

Figure 10. Comparison of the equivalent inversion factor (γ_{eq}), circuit quality factor (Q_I), and equivalent circuit quality factor (Q_{Ieq}) from the theoretical predictions and the simulations conducted in LTspice™ Software: (a) γ_{eq} and (b) Q_I and Q_{Ieq}.

higher efficiency for each voltage inversion process (Tang et al., 2025) and, thereby, an enhanced electrical damping effect.

In Figure 10(a), the equivalent voltage inversion factor γ_{eq} achieved by the SSDBF circuit is also validated by comparing simulation results in LTspice™ with the theoretical results from equation (18). In simulation models, we kept the inductance constant for the SSDI and SSDBF circuit, and identified γ and γ_{eq} by setting different values of the parasitic resistance r, referring to R_1 in Figure 8(a). Similarly, Figure 10(b) compares the simulation and theoretical results of the circuit quality factors Q_I and Q_{Ieq} for the SSDI and SSDBF circuits, which are calculated based on the data of the voltage inversion factors γ and γ_{eq}. The excellent agreement between the simulation and theoretical results confirms that the SSDBF circuit can enhance both the equivalent voltage inversion factor and the circuit quality factor compared to the conventional SSDI circuit. Moreover, the accuracy of the derived theoretical equations is verified under the assumption that the three bias-flips share a unified voltage inversion factor γ.

The impact of the bias capacitor C_b on the dynamics of the SSDBF circuit is investigated by simulating the system response from initially at rest to steady state under an open-circuit resonant frequency and an excitation acceleration of $0.1g$. Figure 11 presents the simulation results of the stabilized time t_s, stabilized bias voltage V_b, and the corresponding bias energy E_b under different values of bias capacitor C_b. As shown in Figure 11(a), a smaller bias capacitor C_b would allow the bias voltage V_b to stabilize in a shorter time, enhancing the response speed of the SSDBF circuit. However, a too small C_b may compromise system robustness. Conversely, a larger C_b would slow down the convergence to a steady state but enhance system stability and

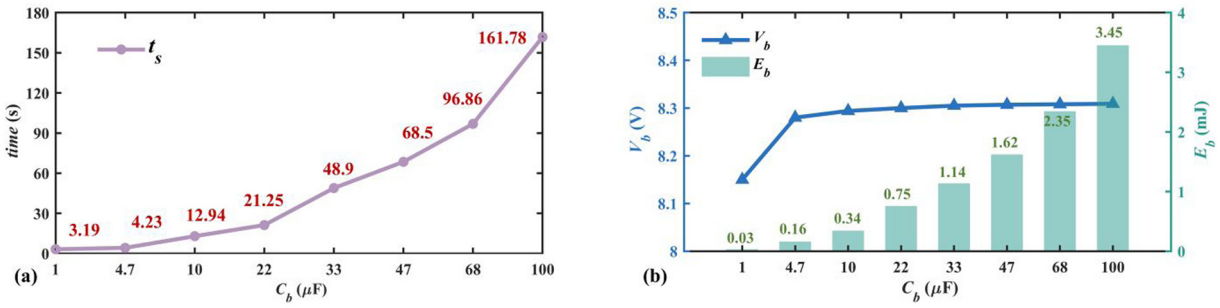

Figure 11. Stability analysis for different bias capacitors: (a) stabilized time t_s and (b) stabilized voltage V_b and the corresponding bias energy E_b.

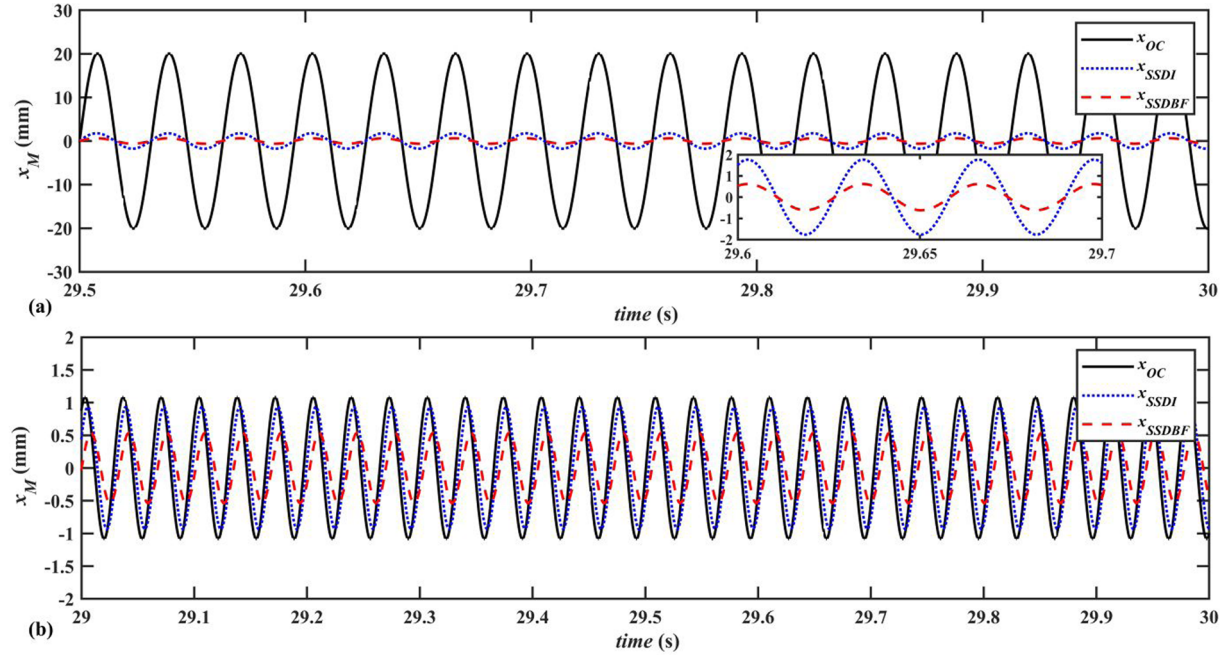

Figure 12. The steady-state displacement waveforms of the electromechanical oscillators connected to the SSDI and SSDBF circuits obtained from LTspice™ simulation: (a) displacement waveforms at the open-circuit resonant frequency (Ω = 1.01) and (b) displacement waveforms at the off-resonate frequency (Ω = 0.95).

robustness by storing more energy, as indicated by Figure 11(b). Moreover, the stabilized bias voltage V_b remains nearly constant across a wide range of C_b, except for a slight reduction when C_b = 1μF. The observation demonstrates that the improved performance of the SSDBF circuit is independent of C_b as long as $C_b >> C_p$ is satisfied.

Figure 12 compares the simulation displacement responses of the SSDI and SSDBF circuits in the steady state under a 0.5*g* acceleration and two different frequencies. The result under the open-circuit condition is also included for reference. Figure 12(a) presents the simulation results at the open-circuit resonant frequency. Compared to the open-circuit condition, x_M significantly decreases when the SSDI/SSDBF circuit is connected to the electromechanical oscillator. Specifically, x_{M_OC} = 20.06 mm in the open-circuit condition and decreases to x_{M_SSDI} = 1.77 and x_{M_SSDBF} = 0.62 mm when the SSDI and SSDBF circuits are used. In addition, an off-resonant (Ω = 0.95) case study is also conducted, with the results shown in Figure 12(b). In this scenario, x_M for the OC, SSDI, and SSDBF circuits are 1.08, 0.93, and 0.54 mm, respectively. Although the vibration attenuation performance is reduced, the SSDBF circuit still exhibits a greater capability than the SSDI circuit, showcasing its excellent adaptivity. Moreover, larger phase lags between the waveforms are observed in the off-

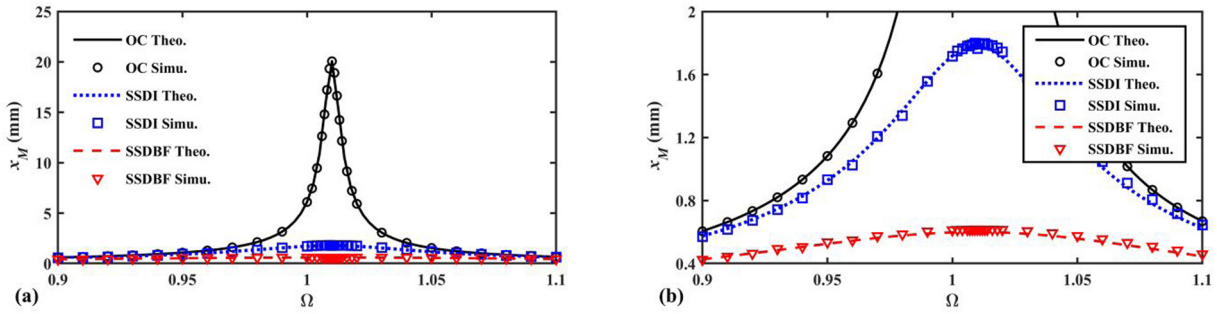

Figure 13. Comparison of the displacement amplitudes of the electromechanical oscillators connected to the open circuit (OC), SSDI circuit, and SSDBF circuit from theoretical predictions and the simulation in LTspice™ Software: (a) general view and (b) enlarged view.

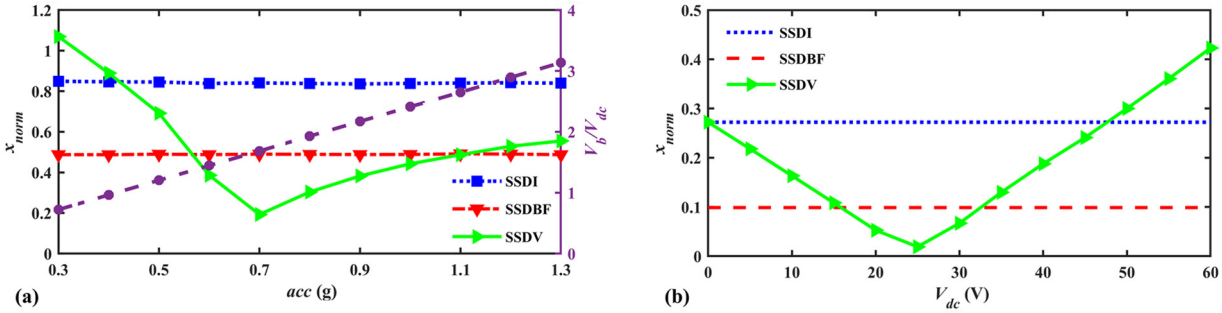

Figure 14. Comparison of the normalized displacement amplitudes of the electromechanical oscillators connected to the SSDI, SSDBF, and SSDV circuits: (a) x_{norm} and V_b/V_{dc} verse excitation acceleration, $\Omega = 0.95$ and (b) x_{norm} versus V_{dc}, $\Omega = 1$, acc = 0.5.

resonant case, which is consistent with the principles of fundamental dynamics.

Furthermore, the frequency responses of the displacement amplitude for the OC, SSDI, and SSDBF circuits based on theoretical results predicted by the developed theoretical model and simulation results from LTspice™ are compared in Figure 13. In the near-resonance frequency region, both the SSDI and SSDBF circuits exhibit strong vibration attenuation effects. Though the vibration attenuation effects weaken in the off-resonance region, the SSDBF circuit can still attenuate vibration much better than the SSDI circuit, with no instability issues observed. The theoretical curve for the open-circuit condition matches well with the simulation result. Minor but acceptable deviations are observed for the SSDI and SSDBF circuit cases, which may be attributed to the disturbances of the peak detection circuit. The overall good agreement between the theoretical and simulation results verifies the accuracy of the theoretical model proposed in Section 3. In general, superior performance of the SSDBF circuit is observed in both near- and off-resonance regions without creating instability issues.

To showcase the self-adaptivity of the SSDBF circuit, Figure 14 compares the normalized displacement amplitudes when utilizing the SSDI, SSDBF, and SSDV circuits. In Figure 14(a), the DC voltage source for the SSDV circuit, V_{dc}, is fixed at 30 V, and the normalized frequency is set to $\Omega = 0.95$. At acc $= 0.7g$, the external voltage source can compensate for the electrical dissipation, with the vibration effectively suppressed at a minimum value of $x_{norm} = 0.193$. The enhancement effect provided by the DC voltage source reduces under larger excitations as the electrical dissipation can only be partly compensated when the amplitude of the voltage across the piezoelectric element becomes larger. On the other hand, x_{norm} for the SSDV circuit sharply increases as the excitation acceleration decreases below 0.7. In this scenario, the DC voltage source injects excessive energy into the piezoelectric element, leading to unexpected excitation instead of attenuation. x_{norm} for the SSDV circuit exceeds those of the SSDBF and SSDI circuits at acc $= 0.5g$ and $0.7g$, respectively, and even surpasses 1 at an acceleration of $0.3g$ or lower, indicating that the SSDV circuit excites the electromechanical oscillator to a greater amplitude than in the open-circuit case. This phenomenon reveals the instability risk for the SSDV circuit with a constant bias voltage source, especially in the off-resonance region. In contrast, the SSDI and SSDBF circuits retain their values of x_{norm} around 0.84 and 0.48 across the examined range of excitation

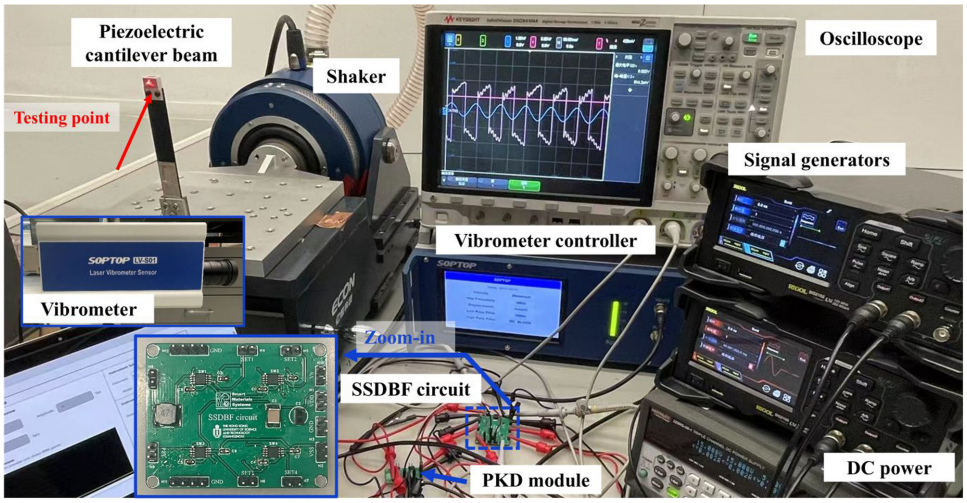

Figure 15. Experimental setup for evaluating the PCB-implemented SSDBF circuit.

accelerations. The ratio of bias voltage V_b to V_{dc} is highlighted as the purple line in Figure 14(a). This ratio keeps rising as the acceleration level increases, indicating that the SSDBF circuit adaptively adjusts V_b to prevent the instability issue.

As shown in Figure 14(b), at $\Omega = 1$ and acc $= 0.5$, the normalized displacement amplitudes corresponding to the SSDI and SSDBF circuits are 0.272 and 0.098, respectively. It is essential to note that the DC voltage is applied only to the SSDV circuit, and the dynamic responses of cases using the SSDI and SSDBF circuits are independent of V_{dc}. Nonetheless, their responses, presented as strictly horizontal lines, are still included to emphasize the instability behavior exhibited by the SSDV circuit. As V_{dc} increases, more energy is injected to amplify the voltage amplitude, and the vibration attenuation effect is strengthened. The minimum x_{norm} occurs at $V_{dc} = 25$ V with a value of 0.019. Beyond this point, the DC voltage source begins to have a counterproductive effect on vibration attenuation, leading to the increase of x_{norm} for the SSDV circuit, which then surpasses those of the SSDI and SSDBF circuits at $V_{dc} = 35$ V and $V_{dc} = 50$ V, respectively. In general, the SSDV circuit outperforms the SSDI circuit when a suitable voltage is applied. In contrast, the SSDBF circuit maintains its superiority, leveraging its self-adaptive ability to tune V_b to accommodate varying excitation conditions.

5. Experimental validation

To validate the enhanced vibration attenuation capability of the proposed SSDBF circuit, experimental tests were carried out on a piezoelectric cantilever beam shunted to an SSDBF circuit implemented on a printed circuit board (PCB).

5.1. Setup description

The experimental platform used to evaluate the SSDBF circuit is illustrated in Figure 15. A fabricated piezoelectric cantilever beam, with an intrinsic capacitance of 68.7 nF and a resonant frequency of 11.54 Hz, is mounted on the shaker (Econ©, EDS). A power amplifier (Econ©, VSA-H102A) drives the shaker, and a vibration controller (Econ©, VT-9002) controls the excitation acceleration through feedback from an accelerometer (Econ©, EV4100). The PCB-implemented SSDBF circuit integrates four analog switch chips (TI©, TMUX6219) to enable bidirectional current flow through the switching branches with a 470 μH inductor and a 10 μF bias capacitor. Switch control signals are generated by two signal generators (RIGOL©, DG2102), which are configured via the upper computer software (RIGOL©, UltraStation). A laser Doppler vibrometer (Soptop©, LVS01) is employed to measure the real-time velocity and displacement of the cantilever beam. A peak detection (PKD) module is utilized to identify the displacement extrema and convert them into rising/falling edge signals, which serve as external triggers for the signal generators to enable synchronized switching control. A DC power supply (KEITHLEY©, 2230G) is used to provide power supplies to the analog switch chips and PKD module. An oscilloscope (KEYSIGHT©, DSOX4104A) is employed to capture and analyze the waveforms of the SSD circuits.

5.2. Waveform analysis

Figure 16 presents experimentally obtained waveforms of the SSDI and SSDBF circuits under an excitation condition of 11.6 Hz and 0.03g. Figure 16(a) and (b) show the waveforms of the piezoelectric voltage V_p and cantilever beam displacement x when the SSDI and

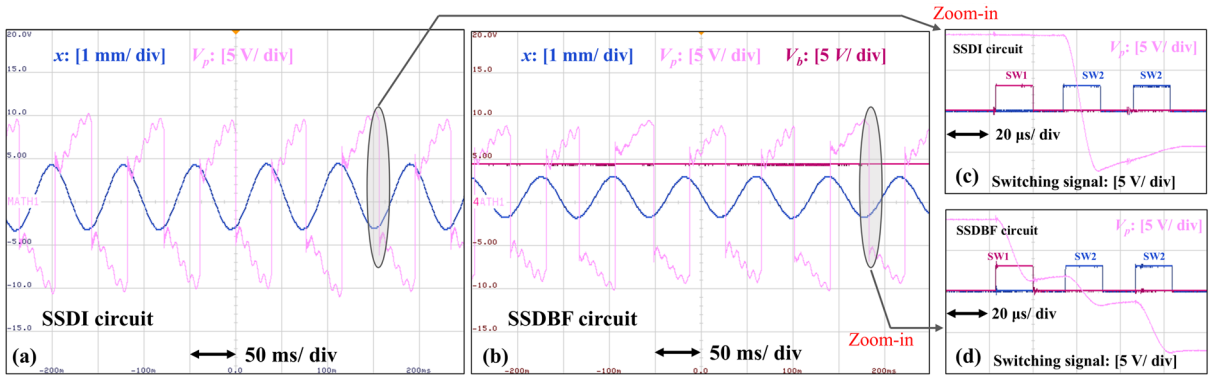

Figure 16. Experimental waveforms: (a) waveforms of piezoelectric voltage V_p and displacement x waveforms for the SSDI circuit, (b) waveforms of piezoelectric voltage V_p, stabilized bias voltage V_b, and displacement x waveforms for the SSDBF circuit, (c) enlarged view at synchronous instants for the SSDI circuit, and (d) enlarged view at synchronous instants for the SSDBF circuit.

SSDBF circuits are respectively used. It can be found that the SSDBF circuit achieves a larger voltage inversion factor. Additionally, the piezoelectric cantilever beam shunted to the SSDBF circuit exhibits a smaller displacement amplitude, as indicated by the blue curves. Moreover, the bias voltage V_b, as indicated by the purple line in Figure 16(b), stabilizes at 4.83 V and remains constant upon reaching a steady state, confirming the quasi-DC behavior of the selected 10 μF bias capacitor, consistent with theoretical predictions. Notably, the piezoelectric voltage rapidly inverts from positive to negative or vice versa at each synchronous instant, effectively introducing impulsive excitations that can stimulate high-order modal responses. These excitations generate high-frequency components that are superimposed onto the fundamental voltage signal and usually appear as sharp peaks immediately following the first inversion event. Such phenomena are commonly observed in synchronous switching circuits and have been reported in previous studies (Lallart, 2022; Long et al., 2023).

Figure 16(c) and (d) show the enlarged views at the synchronous instants for the SSDI and SSDBF circuits, respectively. The control signals for Switch #1 and #2 are indicated by the purple and blue square waveforms, respectively. Notably, the SSDI circuit is implemented on the same PCB as the SSDBF circuit, with the bias capacitor removed to minimize experimental variability. As a result, in the SSDI configuration, the voltage inversion process is achieved through a single LC oscillation triggered by the second switching control signal. In contrast, the proposed SSDBF circuit conducts three sequential bias-flip operations, demonstrating that the employed analog switches are capable of managing the precise timing, which is essential to the SSDBF technique.

During the experiments, the switch-on duration for each LC oscillation was set to 17 μs, and the interval between the two switches was set to 15 μs. The switch-on time must be carefully tuned to be slightly shorter than half of the LC oscillation period. Otherwise, an undesired opposite bias-flip may occur due to the underdamped nature of the LC resonance, causing the piezoelectric voltage to immediately reverse after reaching an extremum. In contrast, the inter-switching interval is less critical and can be adjusted with greater flexibility. As shown in Figure 16(c) and (d), the voltage inversion processes are effectively terminated as soon as the switching control signals end, indicating that the selected analog switch chip, with a turn-on/off time less than 200 ns, provides the timing precision for the SSDBF circuit. Moreover, the use of an analog switch chip enables the SSDBF circuit to be implemented fully in accordance with the proposed topology shown in Figure 3, and the precisely set switch-on time effectively compensates for the absence of diode-based circuitry topologies employed in conventional SSDI and SSDV circuits. Although the induced high-frequency components and the limited peak detection accuracy may affect the performance, the conclusion that the SSDBF circuit outperforms the SSDI circuit remains valid, as all experimental variables were properly controlled.

5.3. Test results

Figure 17(a) and (b) present the measured peak-to-peak displacement amplitude x_{pp} for the SSDI and SSDBF circuits in the experimental test under acceleration levels of 0.05g and 0.08g, respectively. The results clearly show that the SSDBF circuit achieves superior vibration attenuation across the frequency range, particularly in the near-resonant region. For instance, at 11.54 Hz and 0.05g, the displacement amplitude x_{pp} is reduced from 8.22 mm in open-circuit conditions to 2.96 mm with SSDI control, and further to 1.98 mm with the SSDBF circuit. In the off-resonant region, the improvement is less pronounced due to the already low amplitude in the open-circuit case. Specifically, x_{pp} is

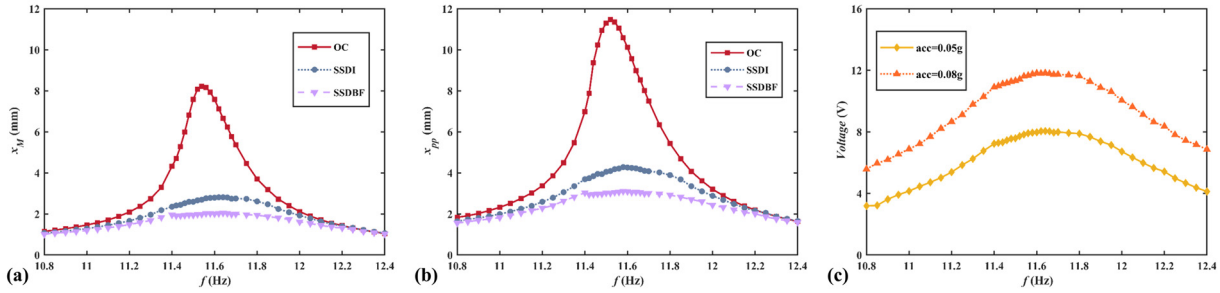

Figure 17. Experimental results of peak-to-peak displacement amplitudes x_{pp} and stabilized bias voltage V_b versus frequency under different excitation conditions: (a) displacement responses for open-circuit, SSDI circuit, and SSDBF circuit under an acceleration of 0.08*g*, (b) displacement responses for open-circuit, SSDI circuit, and SSDBF circuit under an acceleration of 0.05*g*, and (c) stabilized bias voltage of the SSDBF circuit under both excitation levels.

reduced from 2.32 mm (open-circuit) to 1.99 mm (SSDI) and 1.82 mm (SSDBF). Nevertheless, the SSDBF circuit keeps providing enhanced attenuation without any instability occurring. Similar trends are also observed under a higher excitation level of 0.08*g*, accompanied by a consistently higher stabilized bias voltage across the frequency range.

Figure 17(c) illustrates the stabilized bias voltage V_b of the SSDBF circuit under two different excitation levels. It is clearly observed that V_b can automatically adjust in response to varying vibration conditions, increasing with larger vibration excitation and decreasing in off-resonant regions. Specifically, at 11.54 Hz, V_b increases from 7.82 to 11.61 V when the excitation rises from 0.05 to 0.08*g*, while at 11.30 Hz, it rises from 4.15 to 6.88 V. This phenomenon highlights the self-adaptivity of the SSDBF circuit, as the charge accumulated in the bias capacitor is internally sourced from the electromechanical system, rather than supplied externally.

The experimental results qualitatively validate the enhanced vibration attenuation of the proposed SSDBF circuit compared to the conventional SSDI circuit. Its unique three bias-flip working mechanism not only enhances the damping effect but also endows the SSDBF circuit with self-adaptive capability, ensuring system stability under varying excitation conditions. It is worth noting that weak nonlinearity, resembling a softening phenomenon, was observed in the open-circuit frequency response of the piezoelectric structure (Leadenham et al., 2016; Leadenham and Erturk, 2020). However, the nonlinear effect remains minor under the low excitation level applied in the experiments. As such, the use of a linear differential equation for analyzing the SSD circuits remains both appropriate and valid. The slight nonlinearity does not compromise the validity of the experimental conclusion regarding the superior performance of the SSDBF circuit over the SSDI circuit.

6. Conclusion

This paper has proposed a novel bias-flip-based SSD circuit, referred to as SSDBF circuit, for enhanced vibration attenuation. Unlike traditional approaches, the SSDBF circuit operates without requiring external voltage sources and effectively enhances the voltage inversion factor based on the SSDI circuit topology, thereby achieving greater electrical damping. Moreover, the stabilized bias capacitor voltage can automatically adjust in response to varying excitation conditions, endowing the SSDBF circuit with self-adaptivity to eliminate instability issues.

A theoretical model has been developed to extend the analysis for SSD circuits across a wide frequency range, considering the influences of different dimensionless factors such as k_m^2, Q_m, and γ. Theoretical studies show that larger k_m^2 and γ will lead to better vibration attenuation performance for both the SSDI and SSDBF circuits. Moreover, compared to the SSDI circuit, the SSDBF circuit can improve the vibration attenuation effect more significantly for weakly coupled systems with low circuit quality factors. Using the LTspice™ Software, the accuracy of the developed theoretical model has been verified in terms of predicting the voltage inversion factor and displacement amplitude. Both simulation and theoretical models have demonstrated that the SSDBF circuit outperforms the SSDI circuit in both near- and off-resonance regions without creating instability issues.

Analog switch chips have been used to implement the required switching control strategy for the SSDBF circuit, and an experimental platform has been established to evaluate the PCB-implemented SSDBF circuit. The experimental results show that under an excitation condition of 11.54 Hz and 0.05*g*, the SSDBF circuit attenuated the peak-to-peak displacement amplitude to 1.98 mm, compared to 2.96 mm with the SSDI circuit and 8.22 mm under the open-circuit condition. Moreover, the stabilized bias voltage exhibited self-

adaptive behavior across various excitation levels. Specifically, it increased from 7.82 to 11.61 V at 11.54 Hz, and from 4.15 to 6.88 V at 11.00 Hz, as the acceleration rose from 0.05*g* to 0.08*g*. These experimental findings have firmly validated the practical feasibility of the SSDBF circuit and demonstrated its enhanced adaptive vibration attenuation performance.

Future work will focus on developing a more compact and integrated implementation of the SSDBF circuit to enhance its practical applicability and explore its potential across a wider range of application scenarios.

ORCID iD

Guobiao Hu https://orcid.org/0000-0002-1288-7564

Funding

The authors disclosed receipt of the following financial support for the research, authorship, and/or publication of this article: This study was financially supported in part by the National Natural Science Foundation of China (Grant No. 52305135), Guangzhou Municipal Science and Technology Bureau (Grant Nos. SL2023A03J00869, SL2023A04J01741), Guangdong Provincial Key Lab of Integrated Communication, Sensing and Computation for Ubiquitous Internet of Things (Grant No. 2023B1212010007), and Guangzhou Municipal Key Laboratory on Future Networked Systems (Grant No. 024A03J0623).

Declaration of conflicting interests

The authors declared no potential conflicts of interest with respect to the research, authorship, and/or publication of this article.

Data availability statement

Data sharing not applicable to this article as no datasets were generated or analyzed during the current study.

Supplemental material

Supplemental material for this article is available online.

References

Aridogan U and Basdogan I (2015) A review of active vibration and noise suppression of plate-like structures with piezoelectric transducers. *Journal of Intelligent Material Systems and Structures* 26(12): 1455–1476.

Asanuma H and Komatsuzaki T (2020) Nonlinear piezoelectricity and damping in partially-covered piezoelectric cantilever with self-sensing synchronized switch damping on inductor circuit. *Mechanical Systems and Signal Processing* 144: 106867.

Badel A and Lefeuvre E (2016) Nonlinear conditioning circuits for piezoelectric energy harvesters. In: E Blokhina, A El Aroudi, E Alarcon, et al. (eds) *Nonlinearity in Energy Harvesting Systems*. Springer International Publishing. pp.321–359.

Badel A, Sebald G, Guyomar D, et al. (2006) Piezoelectric vibration control by synchronized switching on adaptive voltage sources: Towards wideband semi-active damping. *Journal of the Acoustical Society of America* 119(5): 2815–2825.

Brenes A, Morel A, Gibus D, et al. (2020) Large-bandwidth piezoelectric energy harvesting with frequency-tuning synchronized electric charge extraction. *Sensors and Actuators A Physical* 302: 111759.

Chen Z, Law M-K, Mak P-I, et al. (2017) Fully integrated inductor-less flipping-capacitor rectifier for piezoelectric energy harvesting. *IEEE Journal of Solid-State Circuits* 52(12): 3168–3180.

Du S, Jia Y, Zhao C, et al. (2019) A fully integrated split-electrode SSHC rectifier for piezoelectric energy harvesting. *IEEE Journal of Solid-State Circuits* 54(6): 1733–1743.

Du S and Seshia AA (2017) An inductorless bias-flip rectifier for piezoelectric energy harvesting. *IEEE Journal of Solid-State Circuits* 52(10): 2746–2757.

Gripp JAB and Rade DA (2018) Vibration and noise control using shunted piezoelectric transducers: A review. *Mechanical Systems and Signal Processing* 112: 359–383.

Hu G, Lan C, Tang L, et al. (2022) Dynamics and power limit analysis of a galloping piezoelectric energy harvester under forced excitation. *Mechanical Systems and Signal Processing* 168: 108724.

Javvaji S, Singhal V, Menezes V, et al. (2019) Analysis and design of a multi-step bias-flip rectifier for piezoelectric energy harvesting. *IEEE Journal of Solid-State Circuits* 54(9): 2590–2600.

Ji H, Chen Z, Qiu J, et al. (2018) Superharmonic vibration and its reduction in SSD control by increase of voltage inversion time. *Smart Materials and Structures* 27(8): 085007.

Ji H, Qiu J, Badel A, et al. (2009a) Semi-active vibration control of a composite beam by adaptive synchronized switching on voltage sources based on LMS algorithm. *Journal of Intelligent Material Systems and Structures* 20(8): 939–947.

Ji H, Qiu J, Badel A, et al. (2009b) Semi-active vibration control of a composite beam using an adaptive SSDV approach. *Journal of Intelligent Material Systems and Structures* 20(4): 401–412.

Ji H, Qiu J, Cheng L, et al. (2016) Semi-active vibration control based on unsymmetrical synchronized switch damping: Analysis and experimental validation of control performance. *Journal of Sound and Vibration* 370: 1–22.

Lallart M (2022) High gain, load-tolerant self-powered series–parallel synchronized switching technique for piezoelectric energy harvesting. *IEEE Transactions on Power Electronics* 37(7): 8649–8658.

Lallart M, Badel A and Guyomar D (2008) Nonlinear semi-active damping using constant or adaptive voltage sources: A stability analysis. *Journal of Intelligent Material Systems and Structures* 19(10): 1131–1142.

Leadenham S and Erturk A (2020) Mechanically and electrically nonlinear non-ideal piezoelectric energy harvesting framework with experimental validations. *Nonlinear Dynamics* 99(1): 625–641.

Leadenham S, Moura A and Erturk A (2016) Exploiting material softening in hard PZTs for resonant bandwidth enhancement. In: *SPIE Proceedings* (ed. G Park), Las Vegas, Nevada, United States, 15 April, p.97992F. SPIE.

Lefeuvre E, Badel A, Brenes A, et al. (2017) Power and frequency bandwidth improvement of piezoelectric energy harvesting devices using phase-shifted synchronous electric charge extraction interface circuit. *Journal of Intelligent Material Systems and Structures* 28(20): 2988–2995.

Lefeuvre E, Badel A, Petit L, et al. (2006) Semi-passive piezoelectric structural damping by synchronized switching on voltage sources. *Journal of Intelligent Material Systems and Structures* 17(8-9): 653–660.

Liang J and Chung HS-H (2013) Best voltage bias-flipping strategy towards maximum piezoelectric power generation. *Journal of Physics Conference Series* 476: 012025.

Liang J and Liao W-H (2012) Impedance modeling and analysis for piezoelectric energy harvesting systems. *IEEE/ASME Transactions on Mechatronics* 17(6): 1145–1157.

Liang J, Zhao Y and Zhao K (2019) Synchronized triple bias-flip interface circuit for piezoelectric energy harvesting enhancement. *IEEE Transactions on Power Electronics* 34(1): 275–286.

Li J, Zhang L, Li S, et al. (2023) Active disturbance rejection control for piezoelectric smart structures: A review. *Machines* 11(2): 174.

Liu L, Shang Y, Cheng J, et al. (2020) An efficient interface circuit for miniature piezoelectric energy harvesting with P-SSHC. *Journal of Circuits System and Computers* 29(08): 2020004.

Long Z, Pan Q, Li P, et al. (2023) Direct adaptive SSDV circuit for piezoelectric shunt damping. *IEEE Transactions on Industrial Electronics* 70(4): 4098–4107.

Lu Z, Wang Z, Zhou Y, et al. (2018) Nonlinear dissipative devices in structural vibration control: A review. *Journal of Sound and Vibration* 423: 18–49.

Morel A, Badel A, Wanderoild Y, et al. (2018) A unified N-SECE strategy for highly coupled piezoelectric energy scavengers. *Smart Materials and Structures* 27(8): 084002.

Morel A, Brenes A, Gibus D, et al. (2022a) A comparative study of electrical interfaces for tunable piezoelectric vibration energy harvesting. *Smart Materials and Structures* 31(4): 045016.

Morel A, Brenes A, Gibus D, et al. (2022b) Electrical efficiency of SECE-based interfaces for piezoelectric vibration energy harvesting. *Smart Materials and Structures* 31(1): 01LT01.

Qureshi EM, Shen X and Chang L (2015) Self-powered synchronized switch damping on negative capacitance for broadband vibration suppression of flexible structures. *International Journal of Applied Electromagnetics and Mechanics* 49(1): 105–121.

Qureshi EM, Shen X and Chen J (2014) Vibration control laws via shunted piezoelectric transducers: A review. *International Journal of Aeronautical and Space Sciences* 15(1): 1–19.

Richard C, Guyomar D, Audigier D, et al. (1999) Semi-passive damping using continuous switching of a piezoelectric device. In: *1999 Symposium on smart structures and materials* (ed. TT Hyde), Newport Beach, CA, 2 June, pp.104–111.

Richard C, Guyomar D, Audigier D, et al. (2000) Enhanced semi-passive damping using continuous switching of a piezoelectric device on an inductor. In: *SPIE's 7th Annual international symposium on smart structures and materials* (ed. TT Hyde), Newport Beach, CA, 27 April, pp.288–299.

Sales TP, Rade DA and de Souza LCG (2013) Passive vibration control of flexible spacecraft using shunted piezoelectric transducers. *Aerospace Science and Technology* 29(1): 403–412.

Shareef A, Goh WL, Narasimalu S, et al. (2019) A rectifierless AC–DC interface circuit for ambient energy harvesting from low-voltage piezoelectric transducer array. *IEEE Transactions on Power Electronics* 34(2): 1446–1457.

Shivashankar P and Gopalakrishnan S (2020) Review on the use of piezoelectric materials for active vibration, noise, and flow control. *Smart Materials and Structures* 29(5): 053001.

Tang H, Liu W, Hu G, et al. (2025) Optimized multi-step synchronous electric charge extraction via accurate electrical efficiency analysis. *Smart Materials and Structures* 34(2): 025027.

Tang L and Yang Y (2011) Analysis of synchronized charge extraction for piezoelectric energy harvesting. *Smart Materials and Structures* 20(8): 085022.

Tian W, Zhao Z, Liu W, et al. (2021) Analysis on the power and bandwidth improvement of a frequency-tuning optimized SECE circuit. *Sensors and Actuators A Physical* 332: 113110.

Wang J, Luo L, Yurchenko D, et al. (2025) Equivalent circuit analysis of a nonlinear vortex-induced vibration piezoelectric energy harvester using synchronized switch technique. *IEEE Transactions on Industrial Electronics* 72: 4865–4876.

Wang X, Wang X, Chai H, et al. (2020) Semi-active vibration control of large-scale flexible structure based on fuzzy adaptive SSDV technique. *International Journal of Applied Electromagnetics and Mechanics* 64(1–4): 1199–1206.

Wu Y, Badel A, Formosa F, et al. (2013) Piezoelectric vibration energy harvesting by optimized synchronous electric charge extraction. *Journal of Intelligent Material Systems and Structures* 24(12): 1445–1458.

Wu Y, Li L, Fan Y, et al. (2019) A linearised analysis for structures with synchronized switch damping. *IEEE Access* 7: 133668–133685.

Wu Y, Liu X, Badel A, et al. (2022) Semi-active piezoelectric structural damping adjustment and enhancement by synchronized switching on energy injection technique. *Journal of Sound and Vibration* 527: 116866.

Wu Y, Yuan Q, Ren K, et al. (2024) Bidirectional energy-controlled piezoelectric shunt damping technology and its vibration attenuation performance. *International Journal of Mechanical System Dynamics* 4(1): 63–76.

Yamada K, Matsuhisa H, Utsuno H, et al. (2010) Optimum tuning of series and parallel LR circuits for passive

vibration suppression using piezoelectric elements. *Journal of Sound and Vibration* 329(24): 5036–5057.

Yan B, Yu N and Wu C (2022) A state-of-the-art review on low-frequency nonlinear vibration isolation with electromagnetic mechanisms. *Applied Mathematics and Mechanics* 43(7): 1045–1062.

Zhang F, Li L, Fan Y, et al. (2019) Numerical analysis and experimental verification of synchronized switching damping systems. In: *ASME 2019 Conference on smart materials, adaptive structures and intelligent systems*, Louisville, KY, 9 September, p.V001T03A006. American Society of Mechanical Engineers.

Zhao B, Zhao K, Wang X, et al. (2021) Series synchronized triple bias-flip circuit: Maximizing the usage of a single storage capacitor for piezoelectric energy harvesting enhancement. *IEEE Transactions on Power Electronics* 36(6): 6787–6796.